Journal of Materials Chemistry A

Accepted Manuscript

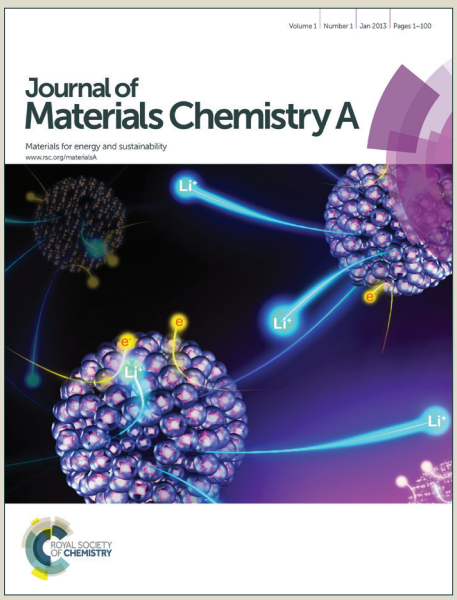

ROYAL SOCIETY OF CHEMISTRY

www.rsc.org/materialsA

A new CO_2-resistant Ruddlesden-Popper oxide with superior oxygen transport: A-site deficient $(Pr_{0.9}La_{0.1})_{1.9}(Ni_{0.74}Cu_{0.21}Ga_{0.05})O_{4+\delta}$

Jian Xue,[a] Qing Liao,[c] Wei Chen,[b] Henny J. M. Bouwmeester,*[b] Haihui Wang,*[cd] and Armin Feldhoff*[a]

[a]*Institute of Physical Chemistry and Electrochemistry, Leibniz University Hannover, Callinstrasse 3A, D-30167 Hannover, Germany*

[b]*Department of Science and Technology, MESA+ Institute for Nanotechnology, University of Twente, 7500 AE Enschede, The Netherlands*

[c]*School of Chemistry & Chemical Engineering, South China University of Technology, No. 381 Wushan Road, Guangzhou 510640, China.*

[d]*School of Chemical Engineering, The University of Adelaide, Adelaide, SA 5005, Australia*

ABSTRACT: A-site deficient $(Pr_{0.9}La_{0.1})_{1.9}Ni_{0.74}Cu_{0.21}Ga_{0.05}O_{4+\delta}$ ($(PL)_{1.9}NCG$), with the K_2NiF_4 structure, is found to exhibit higher oxygen transport rates compared with its cation-stoichiometric parent phase. Stable oxygen permeation fluxes of 4.6×10^{-7} mol·cm^{-2}·s^{-1} at 900 °C at a membrane thickness of 0.6 mm are measured, using either helium or pure CO_2 as sweep gas at a flow rate of 30 ml min^{-1}. The oxygen fluxes are more than two times higher than that observed through A-site stoichiometric $(PL)_{2.0}NCG$ membranes operated under similar conditions. The high oxygen transport rates found for $(PL)_{1.9}NCG$ are attributed to highly mobile oxygen vacancies, compensating A-site deficiency. The high stability against carbonation gives $(PL)_{1.9}NCG$ potential for use, e.g., as membrane in oxy-fuel combustion processes with CO_2 capture.

KEYWORDS: A-site deficiency, K_2NiF_4, oxygen content, CO_2 resistance, oxygen flux

1 Introduction

Clean energy delivery technologies are imperatively required for the purpose of reducing the emission of CO_2 to avert the global climate change. Oxygen-transport membranes (OTMs) based on mixed electronic and ionic conductors have gained increasing attention due to their economical, efficient, and environmentally friendly production of oxygen from air and their potential integration in oxy-fuel technologies with CO_2 capture.[1, 2] In the oxy-fuel process, a part of the flue gas, which contains CO_2, is recycled and used as sweep gas. Therefore, oxygen-transport membranes should not only exhibit a high oxygen flux, but also show a good stability under CO_2-containing atmospheres.[3, 4]

Acceptor-doped perovskite-type oxides $A_{1-x}A_x'B_{1-y}B'_yO_{3-\delta}$ (A, A'= La, Sr, Ba; B, B' = Fe, Co, Nb, etc.) have been investigated extensively as OTMs over the past two decades.[5, 6] The ionic charge carriers created by acceptor-doping are mobile oxygen vacancies. Indeed, high oxygen fluxes are measured for materials with high concentrations of oxygen vacancies: Up to 1/4 of the oxygen sites can be vacant like, for example, $SrCo_{0.8}Fe_{0.2}O_{3-\delta}$ and $Ba_{0.5}Sr_{0.5}Co_{0.8}Fe_{0.2}O_{3-\delta}$.[7, 8] A drawback is that these materials are prone to carbonation. An oxygen-impermeable alkaline-earth carbonate layer will be formed on the membrane surface exposed to the CO_2-containing sweep gas, resulting in a decline of the oxygen permeation flux with time.[9, 10] A-site deficiency is commonly

adopted in an attempt to lower the basicity, thereby increasing the resistance of the membrane material towards carbonation.[11]

Alternatively, problems with a limited CO_2 stability could be avoided by the development of alkaline-earth-free membrane materials. In this regard, perovskite-related Ruddlesden-Popper (RP) $A_{n+1}B_nO_{3n+1}$ materials, in particular those with the K_2NiF_4 structure (the first member of the RP oxides with $n = 1$), are attracting increasing attention.[12, 13] The latter structure consists of alternate AO rock-salt and ABO_3 perovskite-like layers along the crystallographic c-axis, as shown in Fig. 1. Oxygen transport proceeds via migration of oxygen interstitials (O3) in the rock-salt layers.[14, 15] Molecular dynamics (MD) simulations predict an interstitialcy diffusion mechanism, also referred to as a 'knock-on' or 'push-pull' mechanism, involving concerted jumps between interstitial oxygen (O3) and apical oxygen (O2) sites, rather than a direct jump between two interstitial sites.[16] A contribution of vacancy-mediated transport may be considered, but this necessitates the formation of oxygen vacancies. Using atomistic computer simulation, Cleave et al. predicted that all of the vacancy mechanisms studied in La_2NiO_4 exhibit lower activation energies than the interstitial process.[17] Most reported oxides with the K_2NiF_4 structure are, however, oxygen hyperstoichiometric so that in most of these cases the role of mobile interstitials is predominant.[12, 18]

Using *in situ* high-temperature neutron powder diffraction, Yashima et al. provided evidence that indeed the ionic charge carriers in $(Pr_{0.9}La_{0.1})_{2.0}Ni_{0.74}Cu_{0.21}Ga_{0.05}O_{4+\delta}$ ($(PL)_{2.0}NCG$) are oxygen interstitials.[18, 19] It was determined that $(PL)_{2.0}NCG$ exhibits the specific thermal anisotropic temperature factors expected for migration via the interstitialcy mechanism. Interestingly, Ishihara and colleagues found that A-site deficient oxides $Nd_{1.9}(Ni_{0.75}Cu_{0.25})_{0.95}Ga_{0.05}O_4$ and $Pr_{1.9}Ni_{0.75}Cu_{0.25}Ga_{0.05}O_4$ exhibit higher oxygen fluxes than their cation-stoichiometric parent phases.[20, 21] The authors, however, refrained from giving a clear explanation of the role of A-site deficieny on oxygen transport. In this work, we have investigated the influence of A-site deficiency of $(PL)_{2.0}NCG$ on structural parameters, oxygen transport, and stability in CO_2 atmospheres.

2 Experimental

2.1. Preparation

Powders of $(Pr_{0.9}La_{0.1})_{1.9}Ni_{0.74}Cu_{0.21}Ga_{0.05}O_{4+\delta}$ ($(PL)_{1.9}NCG$) and $(PL)_{2.0}NCG$ were prepared by a combined citrate and ethylene-diamine-tetraacetic-acid (EDTA) method as described previously.[22, 23] The as-prepared powders were uniaxially pressed at 20 MPa to obtain green pellets followed by their sintering in air at 1230 °C for 10 h in a bed of the corresponding powder. The density of the sintered disk membranes obtained was measured by the Archimedes method using distilled water. Only membranes with a relative density higher than 95% were selected for permeation experiments. The membranes were polished to the desired thickness using 1200 grit-sandpaper, and then washed with ethanol.

2.2. Structural characterization

The crystal structure of the sintered disks was studied by *in situ* X-ray diffraction (XRD, D8 Advance, Bruker-AXS, with Cu Kα radiation) equipped with a HTK-1200N high-temperature

oven chamber (Anton-Paar). Measurements were conducted under CO_2 atmosphere from 30 to 1000 °C. The temperature was step-wise increased, with a dwell time at each step of 50 min before actual data collection. The oxygen content of $(PL)_{1.9}NCG$ and $(PL)_{2.0}NCG$ in air at 900 °C was evaluated by hydrogen reduction in a thermogravimetric (TGA) apparatus (Netzch TG 449 F3), assuming that the products of hydrogen reduction were Pr_2O_3, La_2O_3, Ni, Cu and Ga.[12, 24] The microstructure of the disk membrane was examined by scanning electron microscopy (SEM) using a JEOL JSM-6700F field-emission instrument operated at an excitation voltage of 2 kV. The elemental composition of the membrane was determined by energy dispersive X-ray spectroscopy (EDXS), using an Oxford Instruments INCA-300 EDX spectrometer with an ultrathin window and at an excitation voltage of 20 kV.

2.3. Oxygen permeation experiments

The oxygen flux through the membranes with different thicknesses was investigated in the range of 800-975 °C using a home-made high-temperature oxygen permeation cell, which is described in detail elsewhere.[25, 26] A commercial ceramic sealant (Huitian, Hubei, China) was used to seal the disk-shaped membrane onto an alumina tube. Synthetic air was fed (150 ml min^{-1}) to the feed side of the membrane, while He or CO_2 gas was fed to the sweep side. Unless specified otherwise a sweep gas flow rate of 30 ml min^{-1} was maintained. Gas flow rates were calibrated with a soap bubble flow meter. The composition of the effluent was analyzed by on-line gas chromatography (GC, Agilent Technologies, 7890A). The leakage of oxygen was subtracted in calculation of the oxygen flux.[25, 27] The contribution of leakage to the apparent oxygen flux was below 0.5 % in all cases.

3 Results and discussion

3.1. Phase analysis and microstructure

Fig. 2 shows the XRD patterns of $(PL)_{1.9}NCG$ and $(PL)_{2.0}NCG$ ceramics after sintering at 1230 °C for 10 h in air. Analysis of the patterns confirms that both materials adopt the tetragonal K_2NiF_4 structure (ICDD PDF number: 01-087-1679). No impurity phases are detected.[28, 29] For a more precise evaluation of the influence of A-site deficiency on the XRD pattern, the reflections at 31.6°, 69° and 79° are magnified and compared in Figs. 2b, c and d, respectively. The 113 reflection of $(PL)_{1.9}NCG$ at 31.6° is slightly shifted to higher 2θ values compared to $(PL)_{2.0}NCG$ as shown in Figure 2b. The 324 and 400 reflections are shifted to higher angle and merge with the 208 reflection, which is shifted to lower angle, as shown in Fig. 2c. Similar phenomenon is found around 79° as shown in Figure 2d, where the 414 and 420 reflections are found to be merged with the 228 reflection. These observations are consistent with the different lattice parameters of $(PL)_{1.9}NCG$ and $(PL)_{2.0}NCG$, which are reported in Table 1.

In-situ XRD measurements were performed on $(PL)_{1.9}NCG$ under pure CO_2 atmosphere from room temperature to 1000 °C. As seen from Fig. 3, no additional reflections are found that would indicate the presence or formation of other phases, e.g., carbonates. The results are consistent with those from our previous study, in which it was found that $(PL)_{2.0}NCG$ also possesses excellent chemical stability under CO_2 atmospheres.[29, 30]

SEM micrographs of the $(PL)_{1.9}NCG$ and $(PL)_{2.0}NCG$ membranes, which were sintered at

1230 °C for 10 h in air, are presented in Fig. 4. As seen from this figure, both membranes show high density. The average grain area estimated from the micrographs is about 51 μm^2 for $(PL)_{1.9}$NCG, which is slightly higher than the value of 42 μm^2 found for $(PL)_{2.0}$NCG. Some fine-grained furnace dust particles are seen in both SEM micrographs. These could be successfully removed by polishing the membranes prior to permeation measurements as was revealed from SEM micrographs recorded after the polishing procedure.

Table 1 lists various properties of $(PL)_{1.9}$NCG and $(PL)_{2.0}$NCG. The unit cell parameters of both materials are close. Compared to $(PL)_{2.0}$NCG, the lattice of $(PL)_{1.9}$NCG has shrinked slightly in the c-axis direction and has expanded slightly in the a-b plane.[31, 32] Furthermore, $(PL)_{1.9}$NCG shows a higher relative density, which might indicate that A-site deficiency enhances the sintering process.[33] The average thermal expansion coefficient of $(PL)_{1.9}$NCG under CO_2 atmosphere is 15.9×10^{-6} K^{-1}, which is slightly higher than the value of 15.1×10^{-6} K^{-1} observed for $(PL)_{2.0}$NCG under the same condition.[30] Note further that the oxygen content of A-site deficient $(PL)_{1.9}$NCG, at 900 °C in air, is significantly less than that observed for A-site stoichiometric $(PL)_{2.0}$NCG. The latter suggests that A-site deficiency is mainly compensated by removal of oxygen from the lattice.

3.2. Oxygen flux

An Arrhenius plot of the oxygen flux through a $(PL)_{1.9}$NCG membrane with thickness 0.6 mm is shown in Fig. 5. Also included are data of oxygen permeation for $(PL)_{2.0}$NCG from our previous study.[29] Similar oxygen fluxes are found whether using He or CO_2 as sweep gas, albeit is that at the lowest temperatures the measured oxygen flux using CO_2 as sweep gas tends to be slightly lower. The latter may be attributed to adsorption of CO_2 molecules at the surface, thereby blocking the surface exhange reaction.[29, 34] Compared to $(PL)_{2.0}$NCG, slightly lower activation energies are found for A-site deficient $(PL)_{1.9}$NCG. Apparent activation energies in the temperature range 800 - 975 °C, using He as sweep gas, are 25 and 27 kJ·mol^{-1} for $(PL)_{1.9}$NCG and $(PL)_{2.0}$NCG, respectively. At 900 °C, the oxygen flux through $(PL)_{1.9}$NCG is 4.6×10^{-7} mol·cm^{-2}·s^{-1} irrespective of the use of CO_2 or He as sweep gas. The observed oxygen flux is more than two times higher than the value of 1.9×10^{-7} mol·cm^{-2}·s^{-1} observed for $(PL)_{2.0}$NCG under the same conditions.[29] A-site cation deficiency thus has a large influence on the oxygen permeability.

The oxygen flux was further investigated as a function of membrane thickness. Oxygen permeation through dense mixed-conducting oxide membranes is governed by bulk diffusion and surface exchange. If bulk diffusion is the rate limiting step, the flux can be described by the Wagner equation,[5, 35]

$$jO_2 = -\frac{RT}{4^2F^2L} \cdot \frac{\sigma_e\sigma_i}{\sigma_e+\sigma_i} \cdot ln\frac{pO_2'}{pO_2''} \qquad (1)$$

where jO_2, R, F, T, L, σ_e, and σ_i denote the oxygen flux, gas constant, Faraday constant, temperature, membrane thickness, and the partial electronic and ionic conductivity, respectively. pO_2' is the oxygen partial pressure maintained at the feed side, while pO_2'' is the oxygen partial pressure at the sweep side. Hence, if the oxygen flux is entirely governed by bulk diffusion, the plot of the normalized oxygen flux, $jO_2 \big/ \ln(pO_2' / pO_2'')$ *versus* reciprocal thickness ($1/L$)

should be linear with the line intersecting the origin. Fig. 6 shows that the normalized oxygen fluxes for both $(PL)_{1.9}NCG$ and $(PL)_{2.0}NCG$ increase proportionally with $1/L$ for thicknesses greater than approximately 1.6 mm ($1/L$ = 0.635 mm^{-1}), but depart from a linear relationship for smaller thicknesses. These results reveal that the oxygen flux is predominantly limited by bulk diffusion for a membrane thickness greater than ~1.6 mm, and by surface exchange for smaller thicknesses.

Since in both $(PL)_{1.9}NCG$ and $(PL)_{2.0}NCG$ the electronic conductivity predominates over the ionic conductivity, Eq. 1 can be simplified to

$$jO_2 = -\frac{RT}{4^2F^2L} \cdot \sigma_i \cdot ln\frac{pO_2'}{pO_2''} \qquad (2)$$

Using this equation, the ionic conductivity was calculated from data of oxygen permeation measurements obtained for 2.3 mm thick membranes. At 900 ^oC, a value of 0.21 $S \cdot cm^{-1}$ is found for A-site deficient $(PL)_{1.9}NCG$, to be compared with 0.10 $S \cdot cm^{-1}$ found for A-site stoichiometric $(PL)_{2.0}NCG$. Increasing the sweep gas flow rate increases the oxygen partial pressure gradient across the membrane. Fig. 7 shows that the oxygen flux measured through a 0.6 mm thick membrane of $(PL)_{1.9}NCG$ at different temperatures increases upon increasing the flow rate of the He sweep gas.

3.3 Stability under CO_2

High oxygen flux and a good chemical stability are two key factors for industrial application of oxygen transport membranes. Good CO_2 resistance was found for the A-site stoichiometric $(PL)_{2.0}NCG$.[29] To assess the stability of A-site deficient $(PL)_{1.9}NCG$ against carbonation, the oxygen permeation performance was studied by periodically changing the sweep gas between He and CO_2. As can be seen from Fig. 8, only a marginal, reversible change of the oxygen flux occurs when the sweep gas is switched back and forth between He and CO_2. Fig. 9 shows the long-term oxygen permeation behavior of the $(PL)_{1.9}NCG$ membrane at 900 and 975 ^oC, using either He or pure CO_2 as sweep gas. Stable oxygen fluxes with no sign of deterioration are observed over 200 h. Comparing the XRD patterns of the $(PL)_{1.9}NCG$ membrane before and after the long-term permeation tests revealed no formation of second phases, as shown in Fig. 10. In particularly, no evidence of carbonation formation was found. Fig. 11 depicts SEM/EDXS images of a cross section of the $(PL)_{1.9}NCG$ membrane after the oxygen permeation tests. The results confirm a homogenous distribution of all elements. The observations confirm the excellent stability of $(PL)_{1.9}NCG$ under CO_2 atmosphere. The observed behavior is in marked contrast with many earth-alkaline containing perovskite oxides whose oxygen permeation fluxes are found to decrease sharply upon CO_2 exposure.[9, 10]

3.4 Influence of A-site deficiency on oxygen transport

Data from this study demonstrate that A-site deficient $(PL)_{1.9}NCG$ shows superior oxygen transport properties compared to A-site stoichiometric $(PL)_{2.0}NCG$. As was mentioned in the introduction, similar observations have been reported by Ishihara and colleagues for A-site deficient $Nd_{1.9}(Ni_{0.75}Cu_{0.25})_{0.95}Ga_{0.05}O_4$ and $Pr_{1.9}Ni_{0.75}Cu_{0.25}Ga_{0.05}O_4$ compared to their A-site stoichiometric forms.[20, 21] The latter authors attributed the phenomenon to grain size effects, increased concentration of interstitial oxygen, or to enhanced diffusivity of interstitial oxygen.[20, 21,

[36] It may be noted that the grain sizes found in this study for $(PL)_{1.9}NCG$ and $(PL)_{2.0}NCG$ are similar (see Fig. 4), while the oxygen hyperstoichiometry decreases rather than increases by introducing A-site deficiency (see Table 1). Clearly other factors must be taken into to account for the observations.

Hydrogen reduction experiments show that, at 900 ^{o}C, $(PL)_{2.0}NCG$ is hyperstoichiometric with $4 + \delta = 4.25$, while $(PL)_{1.9}NCG$ is found to be almost oxygen stoichiometric, $4 + \delta = 3.98$ (Table 1). At the same time the oxygen fluxes through $(PL)_{1.9}NCG$ membranes, in the range 800 - 975^{o}C, exceed those through $(PL)_{2.0}NCG$ membranes by a factor 2-3 (Fig. 5). Interestingly, despite the apparent lowering in ionic charge carrier concentration by introducing A-site deficiency, oxygen transport has increased. The results are taken as evidence that the ionic charge carriers in the $(PL)_{1.9}NCG$ must exhibit a higher diffusivity that overcompensates the loss in ionic charge carrier concentration compared to $(PL)_{2.0}NCG$. As the oxygen content of $(PL)_{1.9}NCG$ is found to be almost stoichiometric, the role of oxygen vacancy diffusion becomes significant. Accordingly, the enhanced oxygen transport observed for $(PL)_{1.9}NCG$ can be accounted for by fast oxygen transport via a vacancy mechanism. Such a conclusion would be consistent with the finding by Cleave et al. that the most likely pathway for oxygen migration in La_2NiO_4, i.e., with the lowest activation energy, is a vacancy mechanism, involving transfer between two apical (O2) sites.[17]

The role of a vacancy mechanism to overall oxygen transport in $(PL)_{1.9}NCG$ can be illustrated by simple defect chemical considerations. The concentration of oxygen vacancies is determined by anion Frenkel disorder. Using standard Kröger-Vink defect notation, this equilibrium can be expressed as

$$O_o^{\times} + V_i \rightleftarrows O_i'' + V_O^{\bullet\bullet} \qquad (3)$$

Close to stoichiometric conditions, i.e., in the regime for dilute defect concentrations, and ignoring defect association, the anti-Frenkel equilibrium constant K_{AF} can be presented as

$$K_{AF} \approx [O_i''][V_O^{\bullet\bullet}] \approx \delta_i \cdot \delta_V \qquad (4)$$

where δ_i and δ_V are the molar fractions of oxygen interstitials and oxygen vacancies, respectively. The overall nonstoichiometry parameter is given by $\delta = \delta_i - \delta_V$. Eq. 4 can be used to calculate δ_i and δ_V provided that K_{AF} is known. Data of such calculation, assuming $K_{AF} = 10^{-2}$, is shown in Fig. 12.

The Nernst-Einstein equation can be used to express the ionic conductivity in terms of the defect concentrations and their diffusivities,

$$\sigma_i = \frac{4F^2}{RTV_m} \cdot (\delta_i D_i + \delta_v D_v) \qquad (5)$$

Where V_m is the molar volume, and D_i and D_v are the diffusivities of interstitials and vacancies, respectively. Eq. 5 can be rewritten into

$$\sigma_i = \frac{4F^2}{RTV_m} \cdot D_i(\delta_i + \delta_v \cdot \xi) \qquad (6)$$

where we defined the parameter $\xi = D_v / D_i$. The relative magnitudes of the diffusivities affect the overall ionic conductivity as is illustrated in Fig. 13. If the defect diffusivities are equal ($\xi = 1$), the ionic conductivity is at minimum at the stoichiometric composition ($\delta = 0$). The plot of the ionic conductivity versus δ obtained for $\xi = 1$ is symmetrical about $\delta = 0$. With increasing ξ, the minimum shifts to higher δ values. In this case a higher ionic conductivity is obtained for hypostoichoimetric ($\delta < 0$) than for hyperstoichiometric ($\delta > 0$) compositions of similar absolute magnitude. It should be emphasized that the value obtained for ξ is determined by the value for K_{AF}. It is easily demonstrated by calculation that, at given value of $K_{AF} = 10^{-2}$, ξ must be 10 to yield a twice higher ionic conductivity for $(PL)_{1.9}NCG$, with δ = -0.02, than for $(PL)_{2.0}NCG$, with $\delta = 0.25$, as is experimentally observed (see Table 1).

In the A_2BO_4 oxides (with the K_2NiF_4 structure), the interstitial oxygen ions O3 are in a tetrahedral environment of the A-site cations as well as of the apical oxygen O2.[15] MD simulations show only a weak dependence of the diffusivity of oxygen interstitials in $Pr_2NiO_{4+\delta}$ with the degree of oxygen hyperstoichiometry.[37] The observations are consistent with MD simulations of oxygen transport in $La_2NiO_{4+\delta}$.[16] Several researchers have investigated the effect of acceptor-doping on the oxygen diffusivity in oxides with the K_2NiF_4 structure. Acceptor doping reduces the concentration of oxygen interstitials. Corresponding results of ^{18}O tracer diffusion studies by secondary-ion mass spectroscopy (SIMS) show the oxygen diffusivities in $La_{2-x}Sr_xNiO_{4+\delta}$ and $La_{2-x}Sr_xCuO_{4+\delta}$ to be suppressed by several orders of magnitudes below the diffusivities for the undoped materials.[12, 38-41] For small Sr additions, the observations are explained by the concomitant decrease in the concentration of oxygen interstitials.[12, 41] For the higher Sr additions ($x \leq 0.2$), where charge compensation of the acceptor dopant occurs, in part, by the formation of oxygen vacancies, these are explained by the occurrence of defect associates $V_o^{\bullet\bullet} - Sr'_{La}$, or vacancy ordering, due to the electrostatic interactions between oppositely charged oxygen vacancies and dopant cations. These findings are in apparent contrast with those from the present work. Assuming that, on the introduction of A-site deficiency, A-site cation vacancies (V'''_{Pr}) and oxygen vacancies are formed, defect associates in $(PL)_{1.9}NCG$ are likely on the basis of simple charge considerations. The high oxygen transport rates observed in $(PL)_{1.9}NCG$, however, provide no evidence of their detrimental influence on ionic conductivity. Our results are believed to have general relevance for optimizing the ionic conductivity of A_2BO_4 oxides by tuning the A/B-site stoichiometry.

4 Conclusions

$(PL)_{1.9}NCG$ has been studied with a view to determining the effects of A-site deficiency on structural parameters, oxygen transport and stability under CO_2 atmospheres. $(PL)_{1.9}NCG$ is found to exhibit higher oxygen transport rates compared with its cation stoichiometric parent phase. The high oxygen transport rates are attributed to highly mobile oxygen vacancies, charge compensating cationic vacancies. The high structural stability towards carbonation gives

$(PL)_{1.9}NCG$ potential for use as membrane, e.g., in oxy-fuel combustion processes with CO_2 capture. As exemplified in this work, the concept of A-deficiency can be used to optimize oxygen transport in layered A_2BO_4 oxides (with the K_2NiF_4 structure).

Acknowledgments

J.X. acknowledges financial support by the China Scholarship Council (CSC), National Science Fund for Distinguished Young Scholars of China (No. 21225625) and the Australian Research Council (ARC) through the Future Fellow Program (FT140100757). Financial support by the German Research Foundation (DFG) (No. FE928/7-1) is appreciated. The authors also greatly acknowledge O. Ravkina, A. Schulz and F. Steinbach for technical support.

Notes and references

1 J. D. Figueroa, T. Fout, S. Plasynski, H. McIlvried and R. D. Srivastava, *International Journal of Greenhouse Gas Control*, 2008, 2, 9-20.

2 C. Gough, *International Journal of Greenhouse Gas Control*, 2008, 2, 155-168.

3 R. Kneer, D. Toporov, M. Förster, D. Christ, C. Broeckmann, E. Pfaff, M. Zwick, S. Engels and M. Modigell, *Energy and Environmental Science*, 2010, 3, 198-207.

4 X. Tan, K. Li, A. Thursfield and I. S. Metcalfe, *Catalysis Today*, 2008, 131, 292-304.

5 J. Sunarso, S. Baumann, J. M. Serra, W. A. Meulenberg, S. Liu, Y. S. Lin and J. C. Diniz da Costa, *Journal of Membrane Science*, 2008, 320, 13-41.

6 K. Zhang, J. Sunarso, Z. Shao, W. Zhou, C. Sun, S. Wang and S. Liu, *RSC Advances*, 2011, 1, 1661-1676.

7 L. Qiu, T. H. Lee, L. M. Liu, Y. L. Yang and A. J. Jacobson, *Solid State Ionics*, 1995, 76, 321-329.

8 Z. Shao, W. Yang, Y. Cong, H. Dong, J. Tong and G. Xiong, *Journal of Membrane Science*, 2000, 172, 177-188.

9 M. Arnold, H. Wang and A. Feldhoff, *Journal of Membrane Science*, 2007, 293, 44-52.

10 J. Yi, M. Schroeder, T. Weirich and J. Mayer, *Chemistry of Materials*, 2010, 22, 6246-6253.

11 V. Kharton, A. Kovalevsky, E. Tsipis, A. Viskup, E. Naumovich, J. Jurado and J. Frade, *Journal of Solid State Electrochemistry*, 2002, 7, 30-36.

12 E. Boehm, J. Bassat, P. Dordor, F. Mauvy, J. Grenier and P. Stevens, *Solid State Ionics*, 2005, 176, 2717-2725.

13 M. Yashima, *Journal of the Ceramic Society of Japan*, 2009, 117, 1055-1059.

14 J. M. Bassat, P. Odier, A. Villesuzanne, C. Marin and M. Pouchard, *Solid State Ionics*, 2004, 167, 341-347.

15 L. Minervini, R. W. Grimes, J. A. Kilner and K. E. Sickafus, *Journal of Materials Chemistry*, 2000, 10, 2349-2354.

16 A. Chroneos, D. Parfitt, J. A. Kilner and R. W. Grimes, *Journal of Materials Chemistry*, 2010, 20, 266.

17 A. R. Cleave, J. A. Kilner, S. J. Skinner, S. T. Murphy and R. W. Grimes, *Solid State Ionics*, 2008, 179, 823-826.

18 M. Yashima, H. Yamada, S. Nuansaeng and T. Ishihara, *Chemistry of Materials*, 2012, 24, 4100-4113.

19 M. Yashima, M. Enoki, T. Wakita, R. Ali, Y. Matsushita, F. Izumi and T. Ishihara, *Journal of*

the American Chemical Society, 2008, 130, 2762-2763.

20 T. Ishihara, N. Sirikanda, K. Nakashima, S. Miyoshi and H. Matsumoto, *Journal of The Electrochemical Society*, 2010, 157, B141.

21 A. Kawahara and T. Ishihara, *Electrochemical and Solid-State Letters*, 2010, 13, B76.

22 A. Feldhoff, M. Arnold, J. Martynczuk, T. M. Gesing and H. Wang, *Solid State Sciences*, 2008, 10, 689-701.

23 J. Xue, Q. Liao, Y. Wei, Z. Li and H. Wang, *Journal of Membrane Science*, 2013, 443, 124-130.

24 W. Chen, A. Nijmeijer and L. Winnubst, *Solid State Ionics*, 2012, 229, 54-58.

25 H. Luo, B. Tian, Y. Wei, H. Wang, H. Jiang and J. Caro, *AIChE Journal*, 2010, 56, 604-610.

26 J. Xue, Q. Zheng, Y. Wei, K. Yuan, Z. Li and H. Wang, *Industrial and Engineering Chemistry Research*, 2012, 51, 4703-4709.

27 H. Wang, R. Wang, D. T. Liang and W. Yang, *Journal of Membrane Science*, 2004, 243, 405-415.

28 C. Tablet, G. Grubert, H. Wang, T. Schiestel, M. Schroeder, B. Langanke and J. Caro, *Catalysis Today*, 2005, 104, 126-130.

29 J. Tang, Y. Wei, L. Zhou, Z. Li and H. Wang, *AIChE Journal*, 2012, 58, 2473-2478.

30 Y. Wei, O. Ravkina, T. Klande, H. Wang and A. Feldhoff, *Journal of Membrane Science*, 2013, 429, 147-154.

31 W. Cheikh-Rouhou Koubaa, M. Koubaa, A. Cheikh-Rouhou, W. Boujelben and A. M. Haghiri-Gosnet, *Journal of Alloys and Compounds*, 2008, 455, 67-72.

32 W. Zhou, R. Ran, Z. Shao, W. Jin and N. Xu, *Journal of Power Sources*, 2008, 182, 24-31.

33 K. Shan and X.-M. Guo, *Materials Letters*, 2013, 113, 126-129.

34 X. Tan, N. Liu, B. Meng, J. Sunarso, K. Zhang and S. Liu, *Journal of Membrane Science*, 2012, 389, 216-222.

35 C. Wagner, *Z. Phys. Chem. B*, 1933, 21, 25-41.

36 S. Miyoshi, T. Furuno, O. Sangoanruang, H. Matsumoto and T. Ishihara, *Journal of The Electrochemical Society*, 2007, 154, B57.

37 D. Parfitt, A. Chroneos, J. A. Kilner and R. W. Grimes, *Physical Chemistry Chemical Physics*, 2010, 12, 6834-6836.

38 Z. Li, R. Haugsrud and T. Norby, *Solid State Ionics*, 2011, 184, 42-46.

39 E. J. Opila, H. L. Tuller, B. J. Wuensch and J. Maier, *Journal of the American Ceramic Society*, 1993, 76, 2363-2369.

40 J. Routbort, S. Rothman, B. Flandermeyer, L. Nowicki and J. Baker, *Journal of Materials Research*, 1988, 3, 116-121.

41 S. J. Skinner and J. A. Kilner, *Solid State Ionics*, 2000, 135, 709-712.

Legends

Table 1
Various parameters for $(PL)_{1.9}NCG$ and $(PL)_{2.0}NCG$. Values between parentheses are standard deviations. Experimental data were acquired from sintered or powder obtained from crushed ceramics.

Figure 1
Oxide with tetragonal K_2NiF_4-type of structure (space group I4/mmm). Atomic positions were calculated from ICSD 173422. For clarity only a subset of the interstitial oxygen ions (O3) is shown.

Figure 2
(a) XRD patterns of $(PL)_{1.9}NCG$ and $(PL)_{2.0}NCG$ after sintering at 1230 ^{o}C for 10 h in air, and (b) magnifications of selected regions of the patterns shown in (a).

Figure 3
(a) *In-situ* high-temperature XRD patterns of calcined $(PL_{1.9})NCG$ powder collected during exposure to pure CO_2, and (b) magnified view of the (113) reflection. Diffractograms were recorded in intervals of 100 °C while not all are displayed for clarity reasons.

Figure 4
Surface SEM micrographs of sintered (a) $(PL)_{2.0}NCG$ and (b) $(PL)_{1.9}NCG$ membranes.

Figure 5
Temperature dependence of the oxygen permeation flux for $(PL)_{1.9}NCG$ and $(PL)_{2.0}NCG$, measured using different sweep gases. Data for both materials were collected under similar conditions. The membrane thicknesses are 0.6 mm. Data for $(PL)_{2.0}NCG$ were taken from our previous study.[29] Apparent activation energies are listed in the figure.

Figure 6
Dependence of the normalized oxygen flux on inverse membrane thickness for (a) $(PL)_{1.9}NCG$ and (b) $(PL)_{2.0}NCG$. Data for the latter were taken from our previous study.[29] Note the different vertical scales.

Figure 7
Dependence of the oxygen flux through a 0.6 mm thick $(PL)_{1.9}NCG$ membrane at different temperatures on the He sweep gas flow rate.

Figure 8
Oxygen permeation flux through a 0.6 mm thick $PL_{1.9}NCG$ membrane at 900 and 975 ^{o}C. Data were collected by periodically changing the sweep gas between He and CO_2. Horizontal dashes lines are guides to the eye.

Figure 9

Long-term stability test of the oxygen permeation flux through a 0.6 mm thick $(PL)_{1.9}NCG$ membrane. Data were collected at two different temperatures, using He and CO_2 as sweep gases as indicated in the figure. Horizontal dashed lines are guides to the eye.

Figure 10

XRD patterns of fresh and spent $(PL)_{1.9}NCG$ membrane after long-term oxygen permeation test.

Figure 11

(a) SEM, and (b-g) EDXS images of a cross section of the $(PL)_{1.9}NCG$ membrane after the long-term permeation tests.

Figure 12

Concentration of interstitial oxygen ions (δ_i) and oxygen vacancies (δ_V) as a function of the overall nonstoichiometry parameter $\delta = \delta_i - \delta_V$, calculated using Eq. 4, assuming $K_{AF} = 10^{-2}$. Values for δ, which are indicated on the top scale, refer to $(PL)_{1.9}NCG$ and $(PL)_{2.0}NCG$ (see Table 1).

Figure 13

The influence of oxygen nonstoichiometry on the apparent ionic conductivity calculated for different values of the oxygen vacancy/oxygen interstitial diffusivity ratio $\xi = D_v / D_i$. Values for δ, which are indicated on the top scale, refer to $(PL)_{1.9}NCG$ and $(PL)_{2.0}NCG$ (see Table 1).

Table 1

	ρ_{exp} g/cm^3	ρ_{exp}/ρ_{theo} %	Average grain size (μm^2)	Crystal symmetry (Space group)	Cell parameters (Å)	Average thermal expansion coefficients in 30°C -1000°C under CO_2 (10^{-6} K^{-1})	Oxygen content at 900°C in air
$(PL)_{2.0}$NCG	7.51(5)	96(1)	42(2)	tetragonal I4/mmm	a = b = 3.8305(4) c = 12.5600 (20)	15.1 [Ref. 30]	4.25(2)
$(PL)_{1.9}$NCG	7.40(5)	98(1)	50(2)	tetragonal I4/mmm	a = b = 3.8345(4) c = 12.5547(20)	15.9(6)	3.98(2)

Figure 1

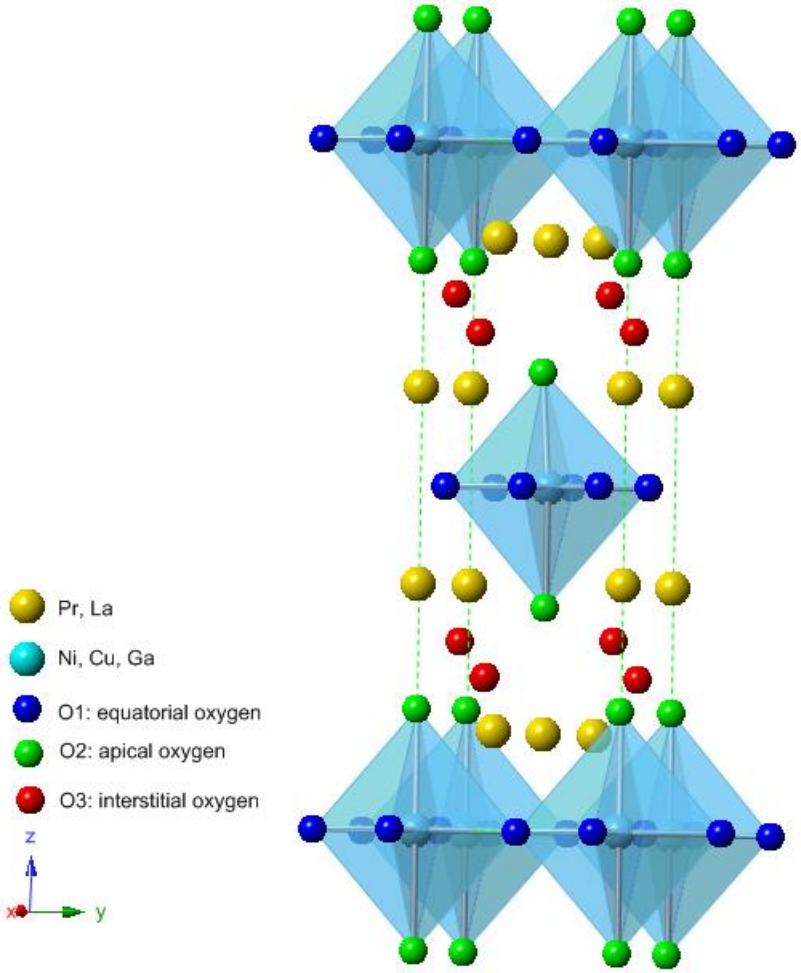

Figure 2

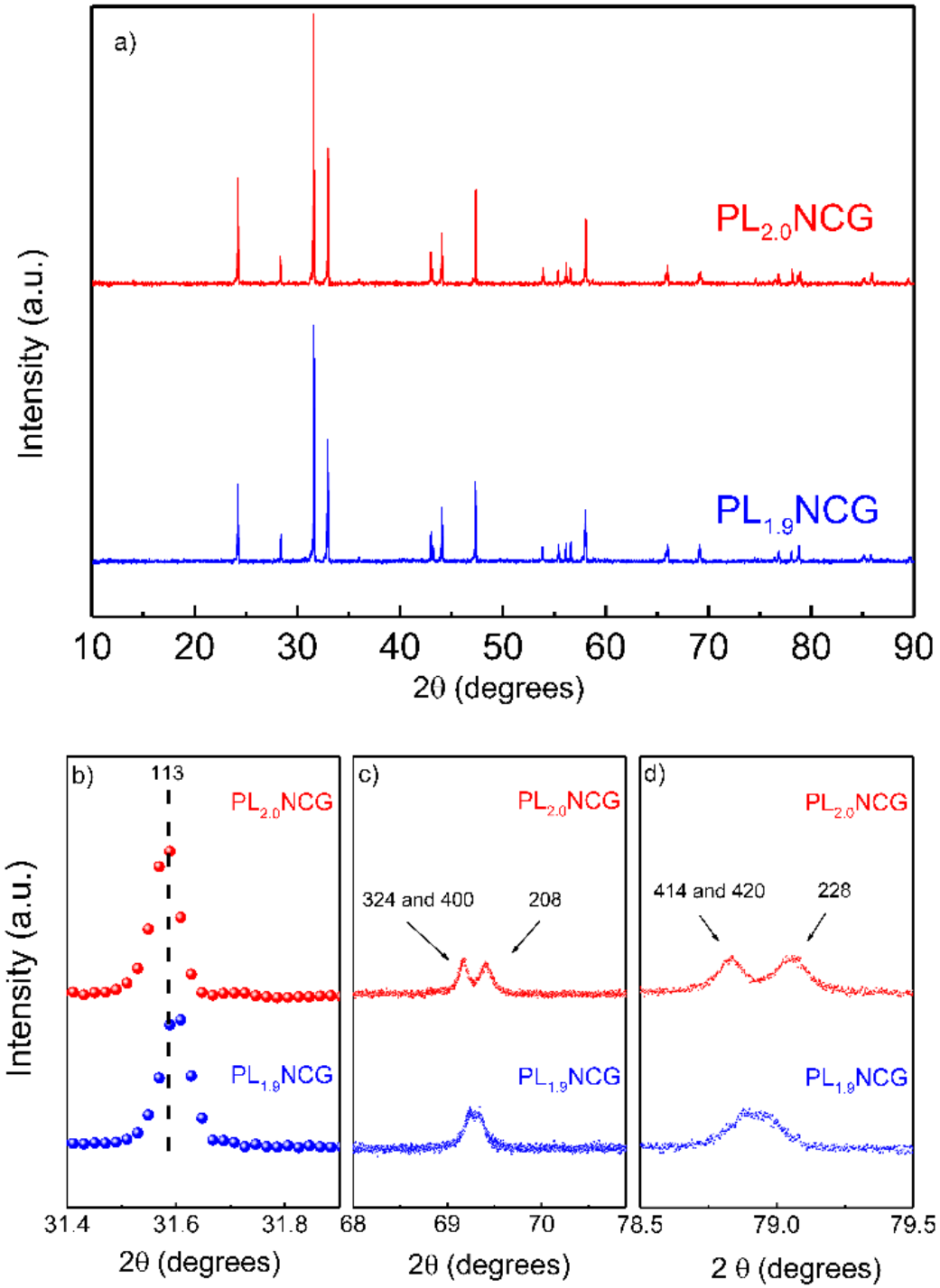

Figure 3

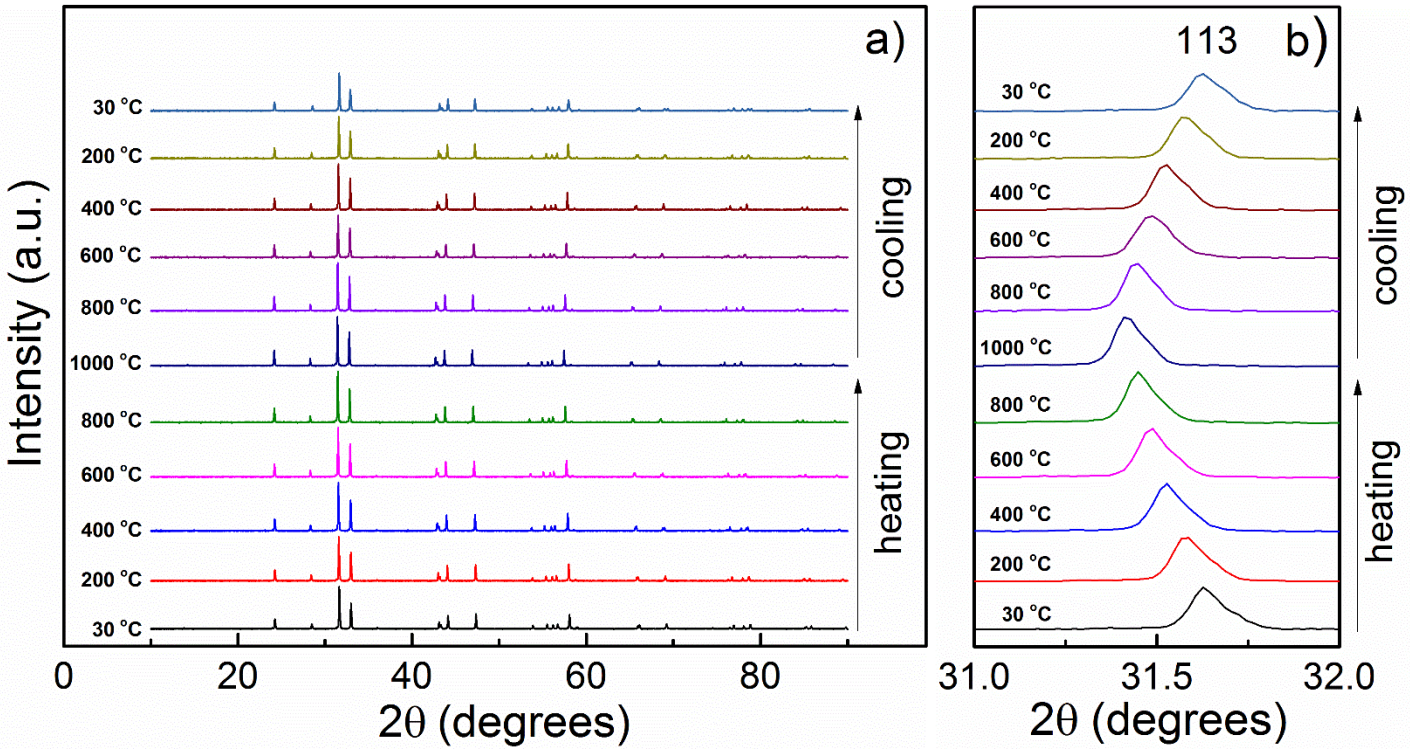

Figure 4

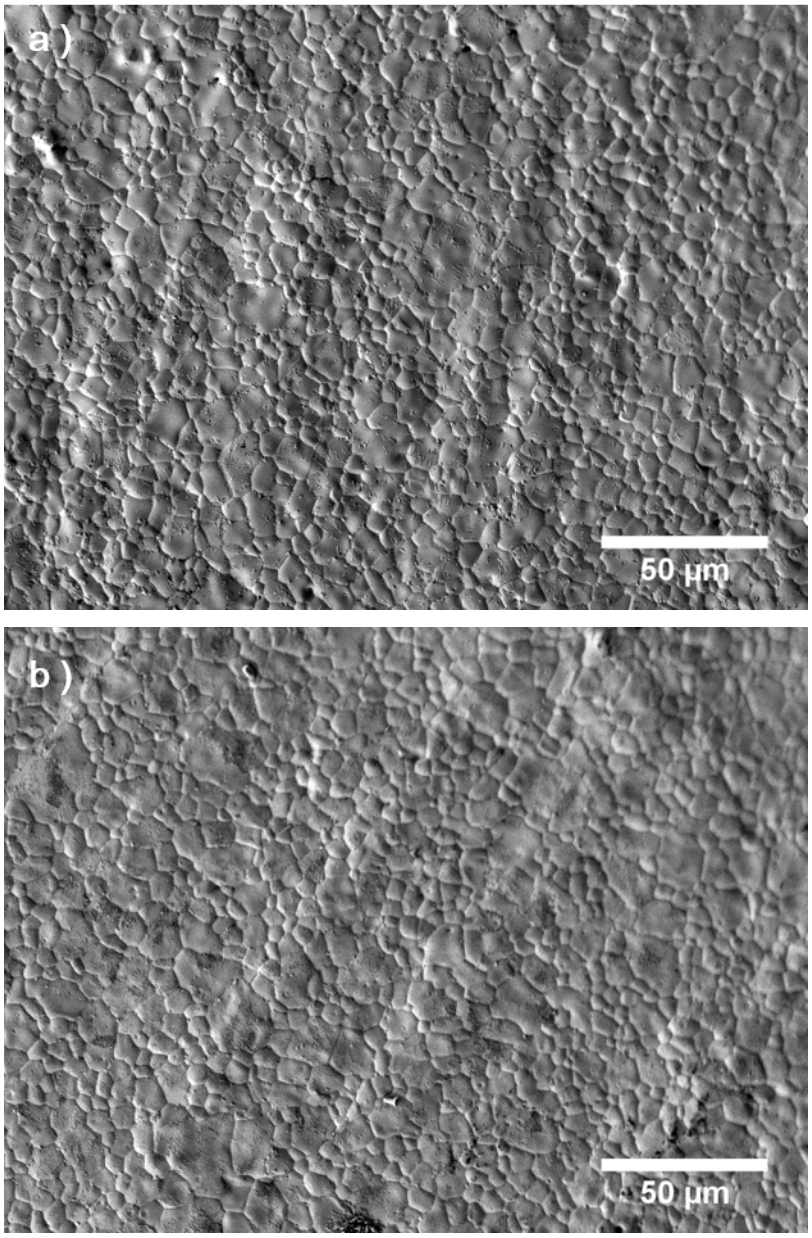

Figure 5

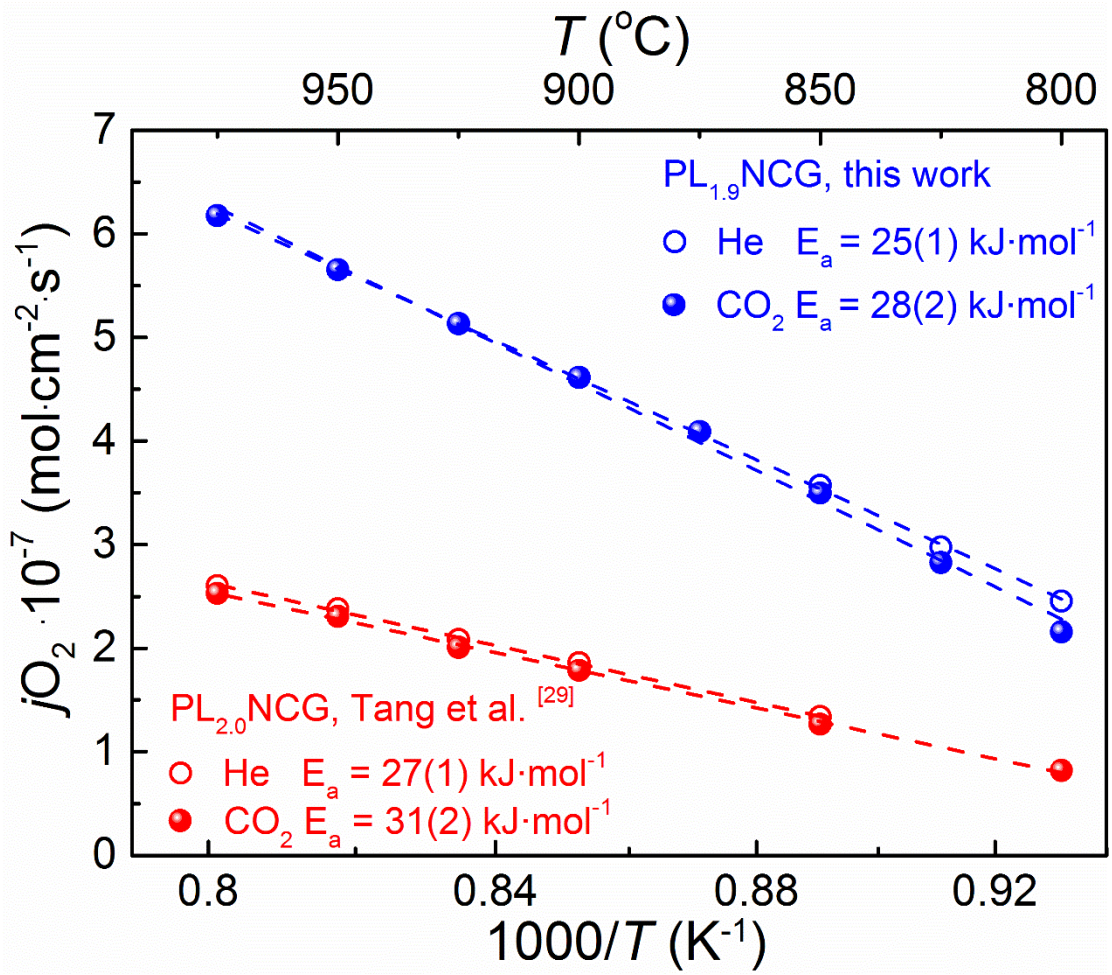

Figure 6

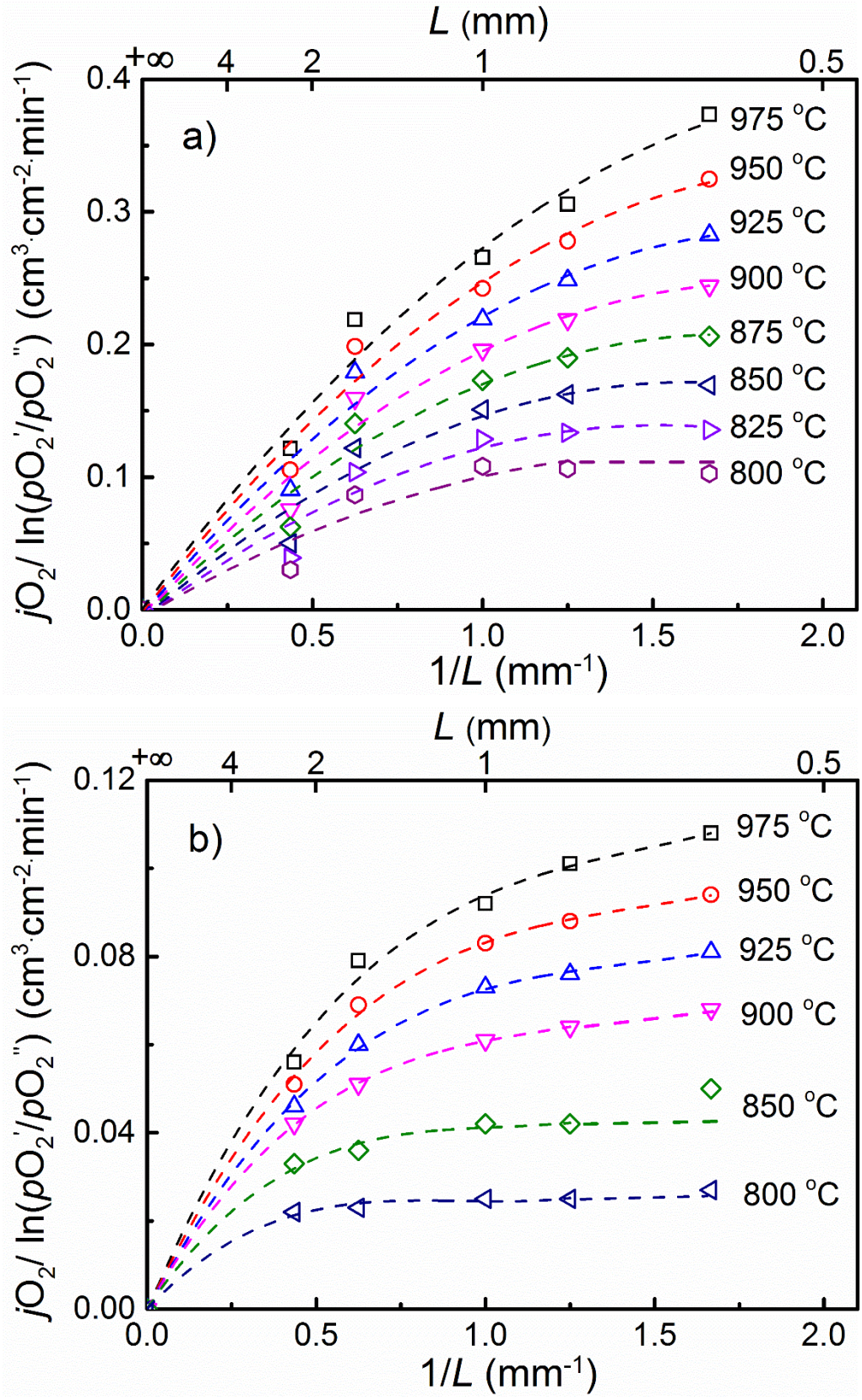

Figure 7

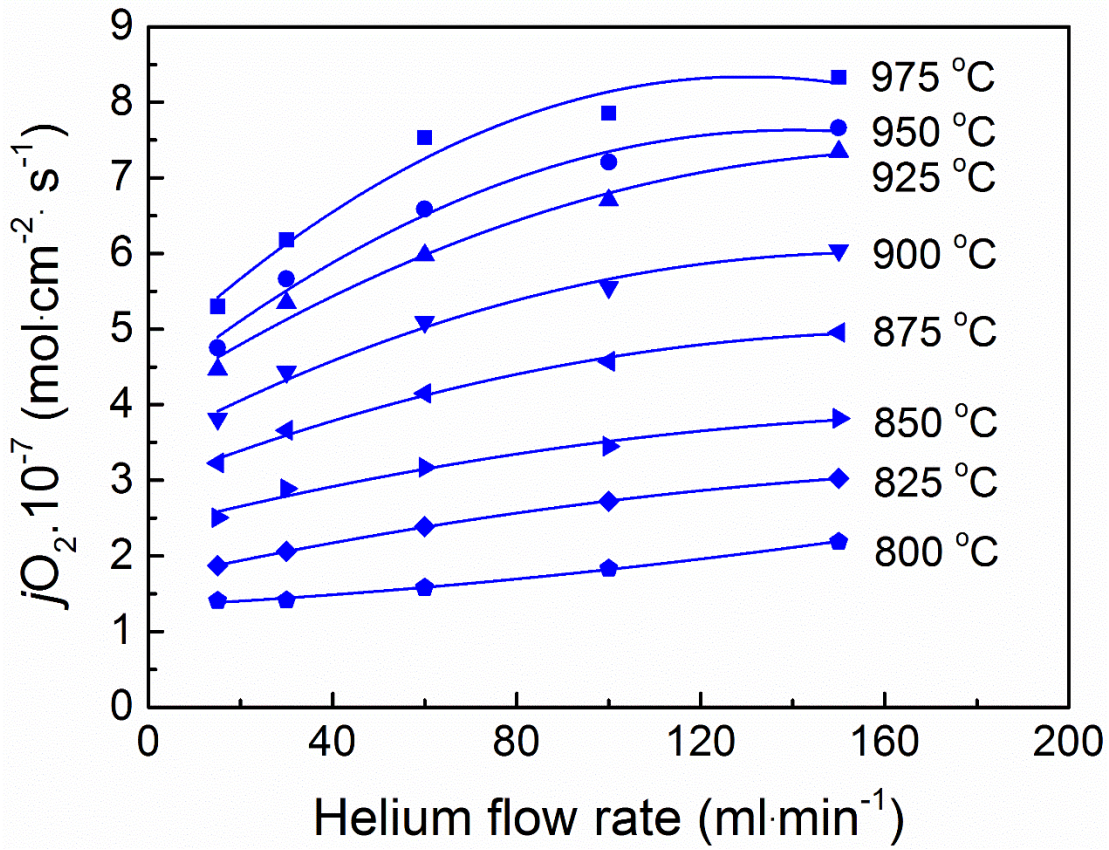

Figure 8

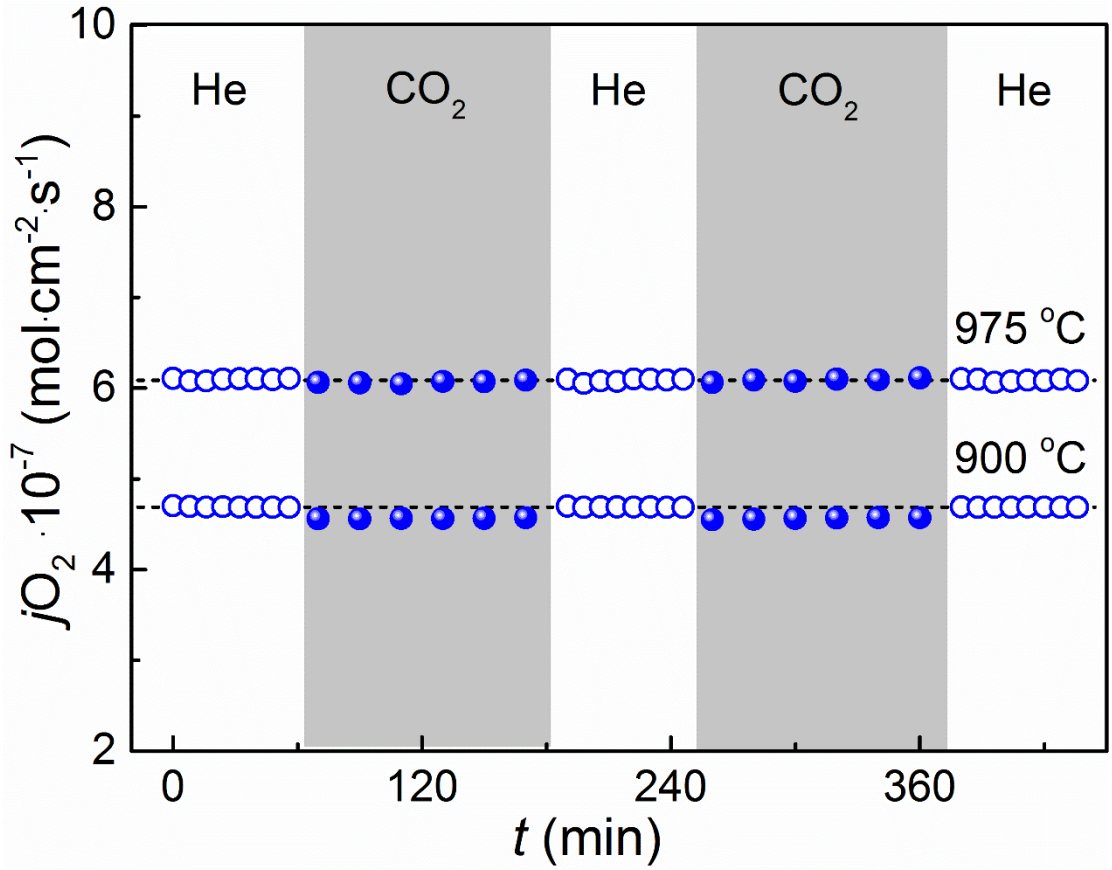

Figure 9

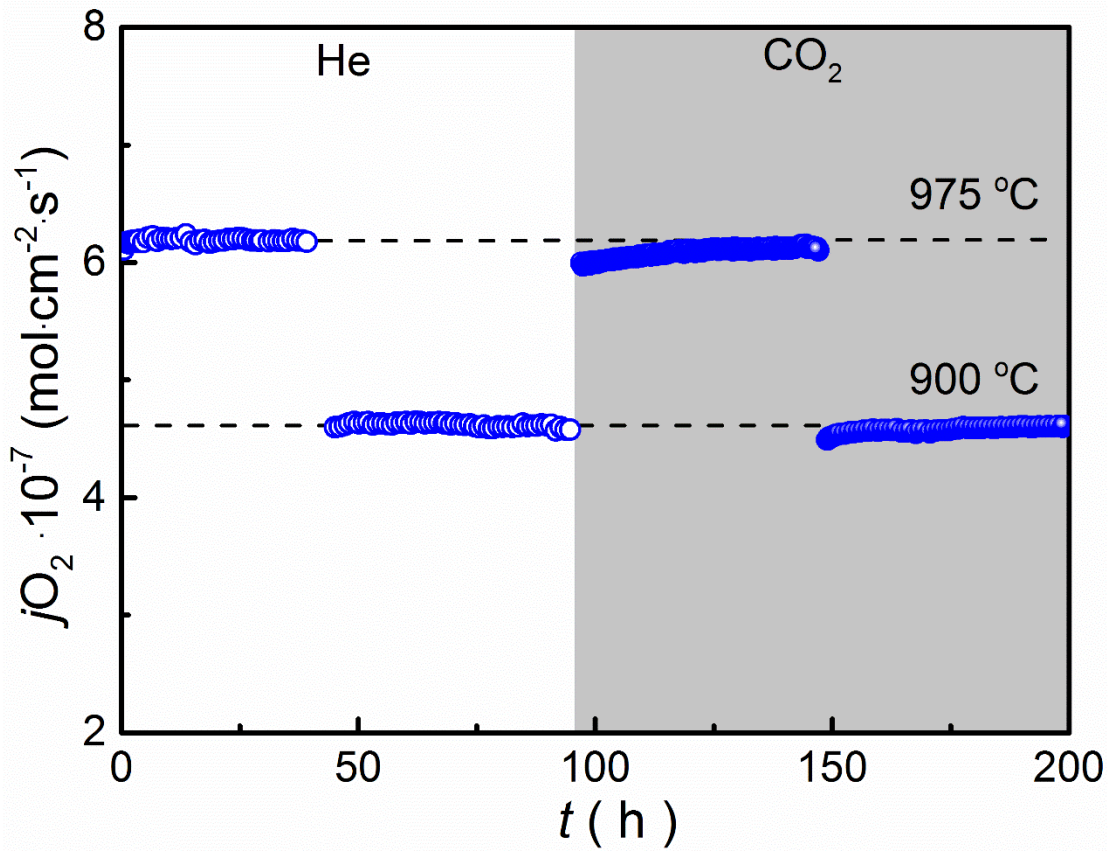

Figure 10

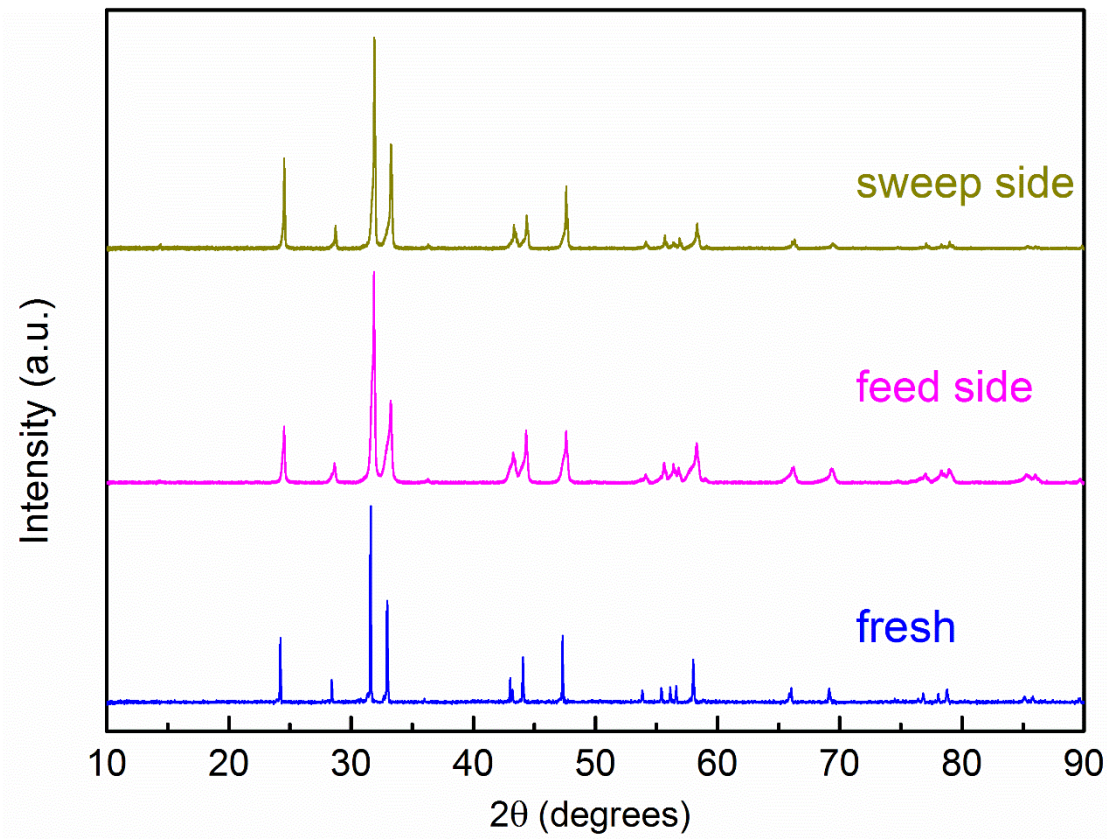

Figure 11

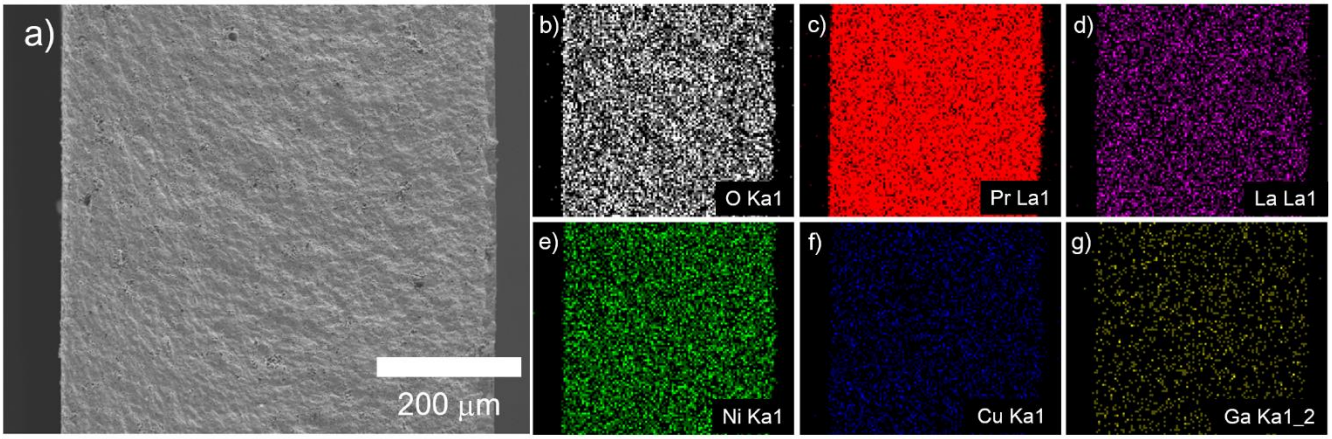

Figure 12

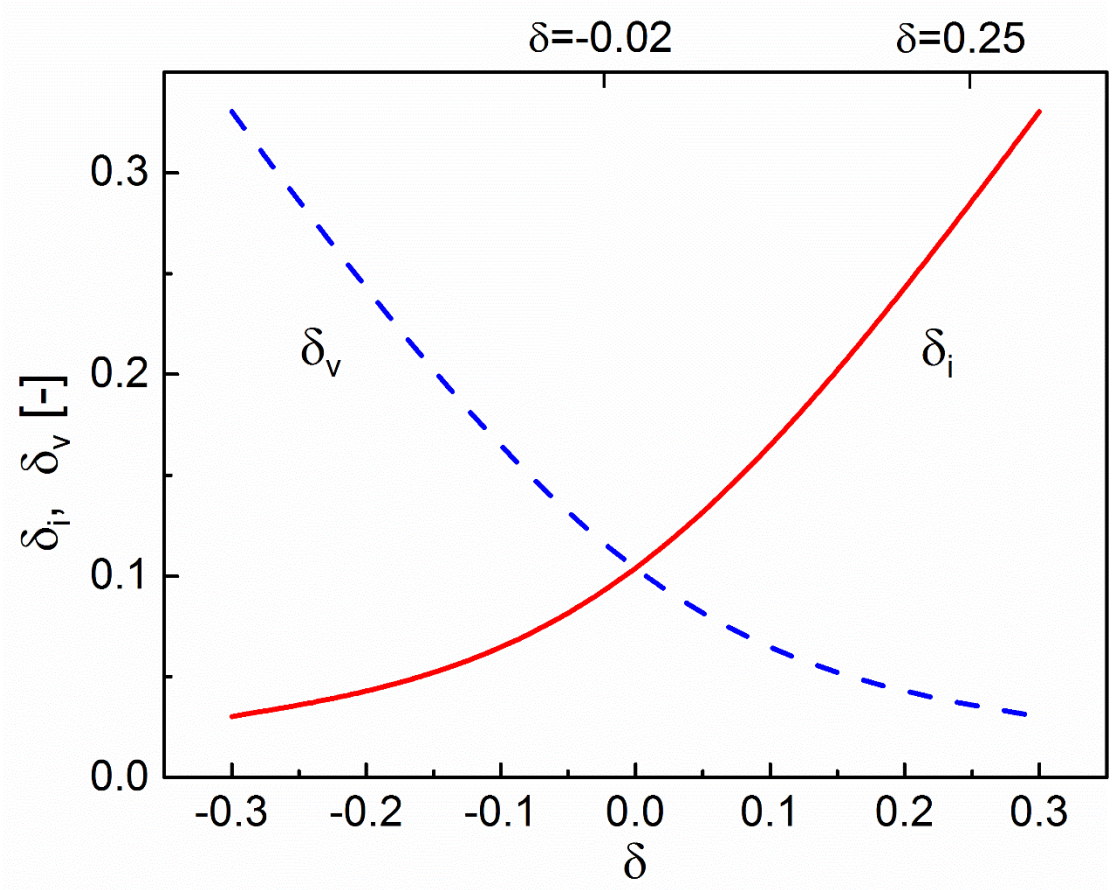

Figure 13